



## OPEN Upper critical fields in normal metal–superconductor–normal metal trilayers

Kelsey B. Robbins<sup>1</sup>, Pukar Sedai<sup>1</sup>, Alexandra J. Howzen<sup>1</sup>, Robert M. Klaes<sup>2</sup>, Reza Loloee<sup>2</sup>, Norman O. Birge<sup>2</sup> & Nathan Satchell<sup>1</sup>✉

The role of spin orbit interaction in superconducting proximity effect is an area of intense research effort. Recent theoretical and experimental works investigate the possible role of spin–orbit interaction in generating spin-triplet pair correlations. In this work, we present an experimental survey of thin normal metal–superconductor–normal metal trilayers with Nb superconductor and Al, Ti, Cu, Pt, Ta, and Au normal metals, along with single layers of Nb as reference. We aim to probe the role of spin–orbit interaction and resistivity on the normal metal proximity effect through measurements of the upper critical field. We find that the upper critical fields of the trilayers are lower than that of a single layer Nb reference sample, and that the trilayers with higher resistivity metals, Ti, Pt, and Ta, behave as 2-dimensional superconductors. At low applied in-plane magnetic fields and temperatures close to the zero field transition temperature, we find a possible deviation from 2-dimensional to 3-dimensional behavior in the Ti and Pt trilayers. We also find that compared to single layer Nb films, all of our trilayers show a greater suppression of critical temperature during rotation from an in-plane to an out-of-plane applied magnetic field, with the greatest suppression observed in trilayers with Au or Al. This suppression of the critical temperature under field rotation might appear analogous to the colossal spin valve effect that can be achieved in systems with ferromagnetic materials; however, in our trilayers, only conventional orbital screening contributions to the suppression are present and the additional suppression is not present in the absence of applied magnetic field.

The superconducting proximity effect occurs when pair correlations from the superconductor proximitize adjacent materials and was first discovered in superconductor–normal metal–superconductor (S–N–S) pressed contacts by Holm and Meissner<sup>1</sup>. For certain N layers, such as Cu, the proximity effect is long-ranged and can occur over several microns<sup>2,3</sup>. Recently, the proximity effect in ferromagnetic materials has received attention due to the generation of spin-triplet correlations by the exchange energy, leading to the field of superconducting spintronics<sup>4–9</sup>. However, most observations of proximity effect in ferromagnetic materials are short-ranged in comparison to proximity in Cu.

Recent Josephson<sup>10–15</sup>, ferromagnetic resonance<sup>16–18</sup>, muon spin rotation<sup>19</sup>, and electrical transport<sup>20–23</sup> experiments have investigated superconductor–ferromagnet heterostructures with additional heavy normal metals, such as Pt, for the possible role of spin–orbit interaction in generating spin-triplets<sup>24–43</sup>, leading to a new field of superconducting spin–orbitronics. For an overview, see the review by Amundsen *et al.*<sup>44</sup> on spin–orbit effects in superconducting hybrid structures.

Early theoretical work studied the upper critical field in S–N systems, assuming that the transparency of the interface was equal to unity<sup>45</sup>. More recent theoretical work has shown that the upper critical field of N–S–N trilayers depends on the transparency of the interface and the normal coherence length for pair correlations<sup>46</sup>. Previous experimental works studied the upper critical fields of Nb–Cu and Nb–Pd systems<sup>47–50</sup>. Layers with large spin–orbit interaction on the surface of thin superconducting layers have recently been predicted to provide a mechanism that can modify and tune the upper critical field<sup>42</sup>. Paschoa *et al.* observed differences in the critical temperature of Nb/Pt bilayers compared to Nb/Cu bilayers under rotation from in-plane to out-of-plane applied magnetic field and interpreted their results as being due to the larger spin–orbit interaction in Pt relative to Cu<sup>51</sup>.

Motivated by observations of spin-triplet proximity effects in systems with heavy normal metals, we present an experimental survey of thin N–S–N trilayers. Nb is the superconducting layer and at 25 nm thickness, the superconductivity in Nb is strongly influenced by the proximity effect in adjacent N layers, which are fixed to a thickness of 15 nm. The chosen N layers are Al, Ti, Cu, Pt, Ta, and Au, to provide both light metals (weaker

<sup>1</sup>Department of Physics, Texas State University, San Marcos, TX 78666, USA. <sup>2</sup>Department of Physics and Astronomy, Michigan State University, East Lansing, MI 48824, USA. ✉email: satchell@txstate.edu

spin–orbit interaction) and heavy metals (stronger spin–orbit interaction). Our choice of materials not only allows us to examine the role of spin–orbit interaction but also allows us to explore the possible role of normal metal resistivity in the proximity effect. We measure the upper critical field of the N–S–N trilayers as a probe of the normal metal proximity effect and explore possible trends.

Our measurements of the upper critical field may offer insight into the mechanism responsible for the breakdown of superconductivity in our trilayers under applied magnetic fields. Several mechanisms can drive this suppression, including conventional orbital screening, Zeeman splitting (Pauli limit), and, in some cases, additional effects from spin–orbit interaction or unconventional superconductivity, such as spin-triplet pairing. Orbital screening occurs when the applied field induces supercurrents that disrupt pair coherence, while the Pauli limit is reached when Zeeman splitting exceeds the superconducting gap, directly breaking spin-singlet pairs. The Pauli limit can be estimated following Clogston and Chandrasekhar as  $B_P \approx 1.84 \times T_c^{52,53}$ . In our samples, we show that orbital screening is the dominant mechanism of the upper critical field for both in-plane and out-of-plane applied fields.

## Results

### Measurements of superconducting transition, $T_c$ and $H_{c2}$

The superconducting transition is characterized using electrical transport measurements. Figure 1 shows measurements on a single layer Nb (25 nm) sample, which we use as a reference and demonstration of how the data on all samples are acquired. Figure 1a shows the resistance as a function of temperature close to the transition for three different out-of-plane applied fields. Figure 1b and c show resistance as a function of applied magnetic field for (b) in-plane and (c) out-of-plane field orientations at fixed temperatures. We extract the critical parameter ( $T_c$  or  $H_{c2}$ ) at the 50% normal state resistance value. There are two methods that we can use to extract the upper critical field of the superconductor with temperature,  $H_{c2}(T)$ . The first, using Fig. 1a, is to extract  $H_{c2}(T)$  from measurements stepping temperature with a fixed magnetic field. Alternatively, we can fix the temperature of the sample and step magnetic field, shown in Fig. 1b and c. The data presented in Fig. 1 demonstrate that both methods provide a consistent value of  $H_{c2}(T)$ . From a practical point of view, we find that the second method has a significantly faster data acquisition time. We use both methods in this study and state which method was used in the relevant section.

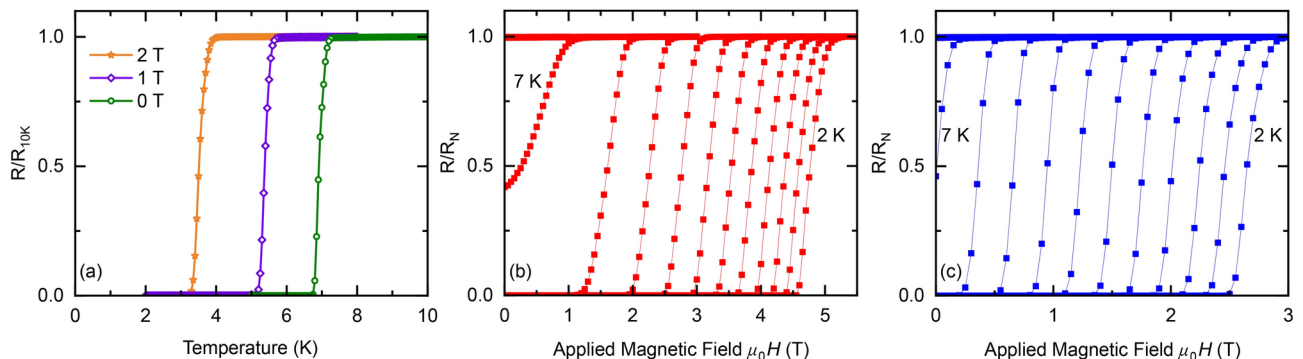
### The upper critical field, $H_{c2}(T)$

Figure 2 shows the extracted  $H_{c2}(T)$  for the eight samples in this study determined by the method shown in Fig. 1b and c. We study two thicknesses of single layer Nb, 25 nm and 55 nm. The 25 nm thick Nb is chosen to match the thickness of the Nb in the N–S–N trilayers and 55 nm thick Nb is chosen to match the total thickness of the trilayer. We study six N–S–N trilayers where the N layers are Al, Ti, Cu, Pt, Ta, and Au, and are fixed at 15 nm thick on either side of the Nb. We follow the same measurement and analysis procedure for all samples in the study. The in-plane and out-of-plane applied field data are considered separately, and the temperature dependence of  $H_{c2}(T)$  in both cases is fit to

$$H_{c2} = H_{c2}(0 \text{ K}) (1 - T/T_c(0 \text{ T}))^\alpha, \quad (1)$$

where  $H_{c2}(0 \text{ K})$  is the extrapolated zero temperature upper critical field and the exponent  $\alpha$  is related to the film dimensionality.

For out-of-plane applied fields,  $\alpha$  is fixed as 1. The zero temperature isotropic coherence length  $\xi_{GL}$  can be estimated from,



**Fig. 1.** Electrical measurements of a 25 nm single layer niobium film for (a) normalized resistance versus temperature at 0, 1, and 2 T out-of-plane magnetic field; (b) normalized resistance versus in-plane magnetic field; and (c) normalized resistance versus out-of-plane magnetic field. Resistance versus magnetic field measurements presented in (b) and (c) were taken at constant temperatures from 2 K in 0.5 K increments. Lines connecting the data are guides.

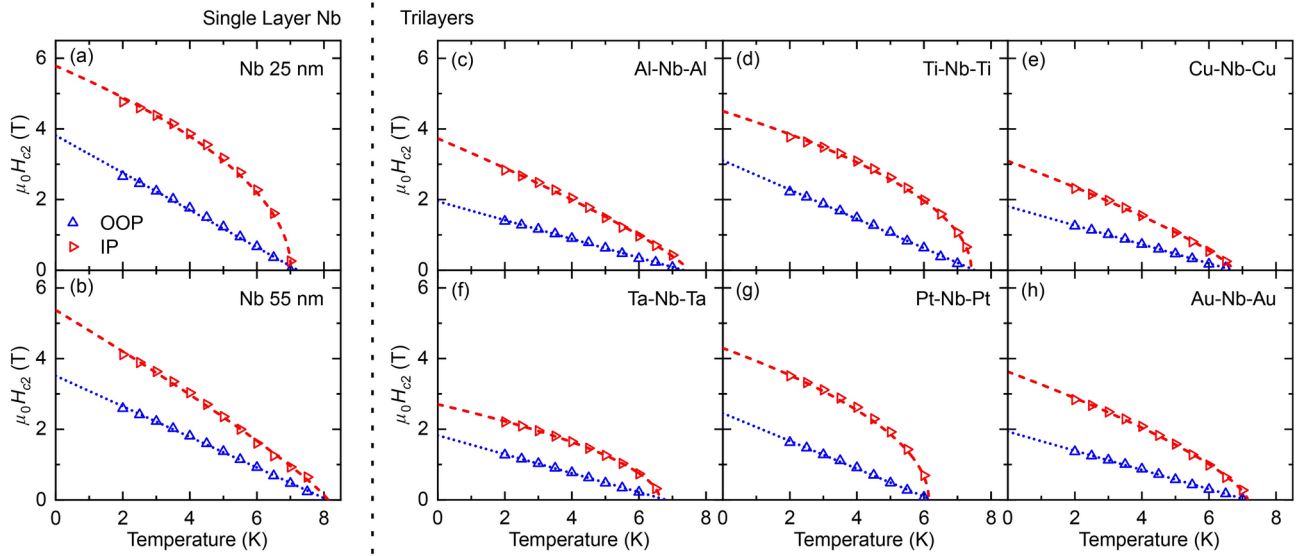


**Fig. 2.** Temperature dependence of the upper critical magnetic field,  $H_{c2}$  for (a) 25 and (b) 55 nm thick, single layer Nb films and for (c) Al–Nb–Al, (d) Ti–Nb–Ti, (e) Cu–Nb–Cu, (f) Ta–Nb–Ta, (g) Pt–Nb–Pt, and (h) Au–Nb–Au trilayer films. The lines represent fits to the Ginzburg–Landau theory, Eq. 1. The best fit parameters are given in Table 1.

Sample	OOP $T_c$ (K)	OOP $\mu_0 H_{c2}$ (T)	OOP $\alpha$ (fixed)	IP $T_c$ (K)	IP $\mu_0 H_{c2}$ (T)	IP $\alpha$ ( $0.5 \leq \alpha \leq 1$ )	$\xi_{GL}$ (nm)	Bulk resistivity ( $\mu\text{Ohm cm}$ )
Nb (25 nm)	$7.23 \pm 0.08$	$3.81 \pm 0.06$	1	$7.02 \pm 0.02$	$5.78 \pm 0.08$	$0.50 \pm 0.02$	9.29	
Nb (55 nm)	$8.11 \pm 0.04$	$3.51 \pm 0.03$	1	$8.1 \pm 0.1$	$5.37 \pm 0.09$	$0.87 \pm 0.05$	9.68	
Al–Nb–Al	$7.34 \pm 0.04$	$1.95 \pm 0.02$	1	$7.5 \pm 0.1$	$3.73 \pm 0.07$	$0.82 \pm 0.04$	13.0	2.74
Ti–Nb–Ti	$7.51 \pm 0.05$	$3.11 \pm 0.03$	1	$7.4 \pm 0.2$	$4.5 \pm 0.1$	$0.50 \pm 0.05$	10.3	43.1
Cu–Nb–Cu	$6.73 \pm 0.03$	$1.81 \pm 0.01$	1	$6.75 \pm 0.05$	$3.09 \pm 0.04$	$0.78 \pm 0.03$	13.5	1.7
Ta–Nb–Ta	$6.82 \pm 0.04$	$1.83 \pm 0.01$	1	$6.63 \pm 0.01$	$2.70 \pm 0.01$	$0.543 \pm 0.007$	13.4	13.1
Pt–Nb–Pt	$6.24 \pm 0.04$	$2.45 \pm 0.03$	1	$6.14 \pm 0.05$	$4.29 \pm 0.09$	$0.50 \pm 0.03$	11.6	10.4
Au–Nb–Au	$7.13 \pm 0.04$	$1.93 \pm 0.02$	1	$7.16 \pm 0.04$	$3.63 \pm 0.04$	$0.70 \pm 0.02$	13.1	2.2

**Table 1.** Best fit parameters of Eq. 1 to the data shown in Fig. 2. The parameters are grouped depending on whether they correspond to fitting the in-plane (IP) or out-of-plane (OOP) applied magnetic field data. The Ginzburg–Landau coherence length,  $\xi_{GL}$ , is estimated from Eq. 2. Bulk resistivity values are reproduced from Kittel<sup>69</sup>.

$$H_{c2}^{OOP}(0 \text{ K}) = \frac{\Phi_0}{2\pi\xi_{GL}^2}, \tag{2}$$

where  $\Phi_0$  is the flux quantum. The best fit parameters and estimated  $\xi_{GL}$  are given in Table 1. For in-plane applied fields, the exponent  $\alpha$  is related to dimensionality.  $\alpha = 1$  for 3D superconductors and  $\alpha = 0.5$  for 2D superconductors, and is a free fitting parameter between those bounds in our analysis. Again, the best fit parameters are given in Table 1.

For the 25 nm thick Nb sample, the best fit returns  $\alpha = 0.50 \pm 0.02$ , consistent with 2D behavior. In the 2D limit of the Ginzburg–Landau model,  $H_{c2}^{IP}(0 \text{ K})$  can be related to the effective thickness of the superconductor,  $d_{\text{eff}}$ , via,

$$H_{c2}^{IP}(0 \text{ K}) = \frac{\sqrt{3}\Phi_0}{\pi d_{\text{eff}}\xi_{GL}}. \tag{3}$$

Using our previously estimated  $\xi_{GL}$ , we estimate  $d_{\text{eff}} = 21 \text{ nm}$ , reasonably consistent with the nominal 25 nm thickness of the Nb layer, particularly since it is known that Nb will form a native oxide and interface layers that decrease the layer’s superconducting thickness<sup>54</sup>. For the 55 nm sample,  $\alpha$  indicates a somewhat intermediate behavior, which is as expected as the thickness of the Nb film is increased. Upon increasing the thickness further, we would expect the Nb film to eventually show the 3D limit,  $\alpha = 1$ .

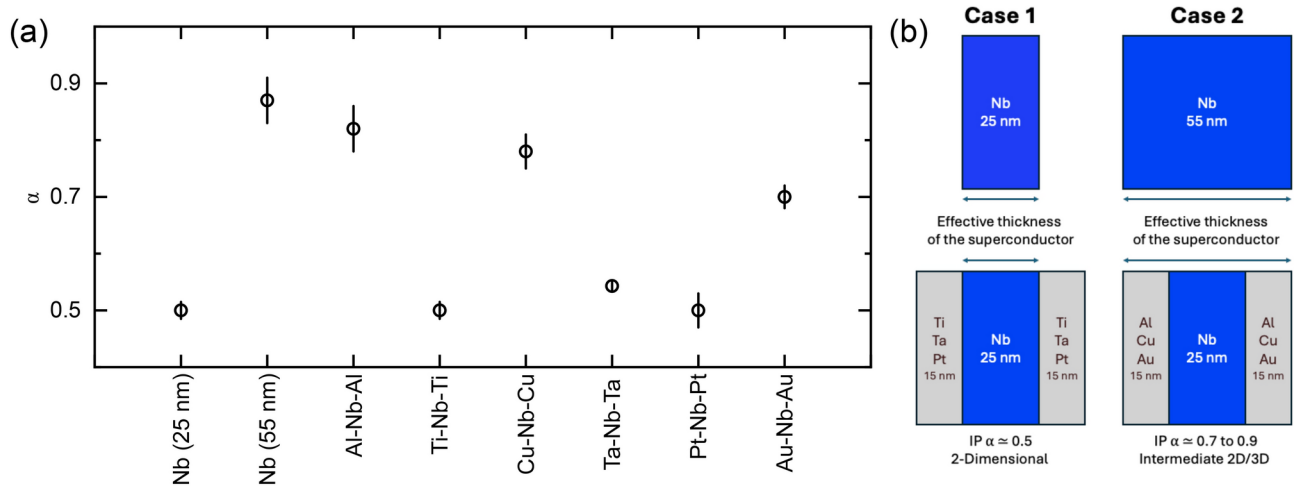


**Fig. 3.** Film dimensionality and effective thickness of the superconductor. **(a)** Extracted film dimensionality parameter,  $\alpha$ , for the fits presented in Fig. 2. In the Ginzburg-Landau theory,  $\alpha = 0.5$  indicates a 2-dimensional superconductor and  $\alpha = 1$  a 3-dimensional superconductor. **(b)** Schematic representation of the effective thickness of the superconductor,  $d_{\text{eff}}$ , based on the comparison of fitted  $\alpha$  and extracted  $d_{\text{eff}}$  between the single layer and trilayer samples.

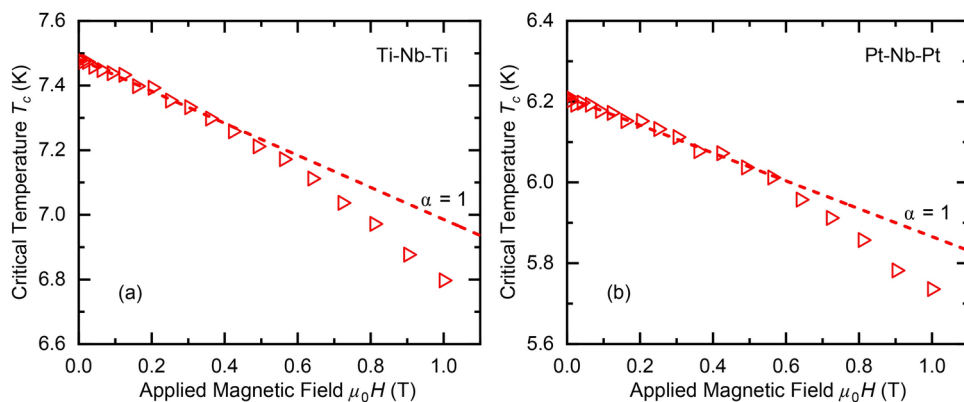


**Fig. 4.** Crossover from 3-dimensional towards 2-dimensional superconductivity at low applied in-plane magnetic fields in the **(a)** Ti-Nb-Ti and **(b)** Pt-Nb-Pt trilayers. The critical temperature is determined at each applied field value by measuring resistance while sweeping temperature at a fixed in-plane magnetic field. The dashed line represents Ginzburg-Landau theory, Equation 4, fit to the lowest field data only ( $\mu_0 H < 0.4$  T) with  $\alpha$  fixed to 1, the 3-dimensional limit.

Having laid out the steps in our data collection and analysis, let us now turn to the N-S-N trilayers, shown in Fig. 2c-h and best fit parameters are again given in Table 1. The proximity effect of normal metals clearly plays an important role in the modification of key parameters ( $T_c$ ,  $H_{c2}$ , and  $\alpha$ ), and these parameters are material dependent. We highlight the material dependence of  $\alpha$  in Fig. 3a.

#### Measurements of superconducting transition at low in-plane fields

We perform further measurements on the Ti and Pt trilayer samples in low in-plane applied magnetic fields to study behavior at  $T$  close to  $T_c$ . We measure the  $T_c$  while varying temperature, following the method shown in Fig. 1a, as this method allows for fine control over fixed low applied magnetic fields. Figure 4 shows the measured critical temperature of the Ti and Pt trilayers for in-plane applied fields. Equation 1 is rearranged to provide  $T_c$  as a function of applied magnetic field,

$$T_c(H) = T_c(0 \text{ T}) \left(1 - (H/H_{c2}(0 \text{ K}))^{1/\alpha}\right), \quad (4)$$

where our new field-dependent parameter  $T_c(H)$  corresponds to the original parameter  $T$  in Equation 1, and  $H$  is the value of the applied magnetic field.

## Discussion

The lateral dimensions of our films greatly exceed the penetration depth of polycrystalline Nb (about 100 nm<sup>54</sup>), but this length scale eclipses the total thickness of our films. For fields applied out-of-plane, the screening currents are in-plane and as a result the upper critical fields are well described by fixing the dimensionality parameter  $\alpha$ , in Equation 1, to 1. For fields applied in-plane, the screening currents are out-of-plane and are strongly influenced by the interaction of the supercurrent with the surfaces and the impedance provided by the S/N interfaces. Based on  $\alpha$ , it is possible to group the behavior of the single Nb layers and the N–S–N trilayers into two categories. The 25 nm Nb layer and the Ti, Ta, and Pt trilayers are in the 2D limit with  $\alpha \approx 0.5$ . The 55 nm Nb layer and the Al, Cu and Au trilayers are in an intermediate regime with  $0.7 \leq \alpha \leq 0.9$ . None of the samples in this study fall into the 3D limit; however, previous work suggests that much thicker 200 nm Nb films can be described by  $\alpha = 1$ <sup>54</sup>.

The dependence of  $\alpha$  appears to correlate with the resistivity of the normal metal in the trilayer. To highlight this trend, we provide the bulk resistivity values for the normal metals in Table 1. The higher resistivity metals, Ti, Ta, and Pt, correspond to the trilayers showing 2D behavior. The 2D behavior of the Ti, Ta, and Pt trilayers suggests that the screening currents are more confined to the Nb layer, and do not spread as much into the normal metals. On the other hand, for the Al, Cu, and Au trilayers, the screening currents occupy the whole thickness of the trilayer. Shown schematically in Fig. 3b, the trilayers can be thought of as having an effective superconducting thickness that is either similar to the thickness of only the Nb layer (Case 1) or similar to the thickness of the entire trilayer (Case 2). Extracting  $d_{\text{eff}}$  from Equation 3 yields 25, 31, and 23 nm for the Ti, Ta, and Pt trilayers, respectively, which is consistent with the interpretation that screening currents are more confined in these trilayers. It is possible that the higher resistivity of Ti, Ta, and Pt suppresses the screening currents in these layers.

The other extracted superconducting parameters,  $H_{c2}$  and  $T_c$ , do not follow the same trend or grouping by material as  $\alpha$ , and do not appear to correlate with the resistivity of the normal metal or the strength of the spin–orbit interaction. For the critical temperature of the trilayer, compared to the single layer Nb film, we expect there to be some competition between an increase in  $T_c$  due to normal metals acting as a capping layer to prevent the oxidation of Nb and the influence due to the proximity effect<sup>46</sup> or spin–orbit interaction<sup>55</sup>. Numerous Nb alloys are known to exhibit intrinsic superconductivity. Given the elevated  $T_c$  observed in our Ti and Al trilayers, it is possible that the formation of alloy layers at the interfaces with these normal metals contributed to the increase in  $T_c$ .

For  $T$  close to  $T_c$ , the expected behavior of thin superconducting films is for the superconductivity to be 2D, as  $\xi$  diverges at high temperatures and exceeds the thickness of the layer<sup>56</sup>. To study whether this expectation holds for the trilayers, we undertake further low field measurements on the Ti and Pt trilayer samples shown in Fig. 4. Our experimental finding is that for  $T$  close to  $T_c$ , the Ti and Pt trilayers are best described by fixing  $\alpha$  to the 3D limit of 1, deviating at higher fields towards 2D behavior. The exact mechanism for this behavior is not known. We note that deviation of  $H_{c2}$  at  $T$  close to  $T_c$  has been previously reported in both thin film and bulk Nb<sup>57,58</sup>.

For the upper critical field, although strong spin–orbit interaction has been shown to increase the in-plane critical field of ultra-thin 2D superconductors<sup>59,60</sup>, we do not see any evidence of such an enhancement of  $H_c$  here. Indeed, for all N–S–N trilayers, the upper critical fields are lower than that of the single layer Nb films we study as reference. Over the range of temperatures we study, we do not observe any signatures suggesting modification or tuning of the upper critical field by spin–orbit interaction<sup>42</sup>, as the data are well described by Equation 1. Revisiting the mechanisms responsible for the breakdown of superconductivity: for our 25 nm-thick Nb, the estimated Pauli limit is 13 T, which is much higher than the largest critical fields measured in our samples. This suggests that, within the applied field range of this study, superconductivity is primarily suppressed by orbital screening. There also does not appear to be a correlation between  $T_c$  and  $H_{c2}$ . For example, the Pt trilayer has a  $T_c$  that is significantly lower than the other trilayers, but the second highest  $H_{c2}$  behind only the Ti trilayer, which has the highest  $T_c$ .

In superconducting systems containing ferromagnetic materials, the spin valve effect is the suppression or enhancement of the critical temperature ( $T_c$ ) by rotating two (or more) ferromagnetic layers with respect to each other from a parallel to antiparallel or perpendicular alignment<sup>61–65</sup>. In the perpendicular alignment, the suppression of  $T_c$  is due to the generation of spin-triplets. The spin valve effect manifests at zero applied magnetic field, provided that the anisotropy of the ferromagnets is sufficient to maintain alignment at remanence. One experimental realization is performed by rotating the sample from field applied in-plane to out-of-plane to achieve a perpendicular magnetic alignment<sup>66–68</sup>. In the previous work of Singh *et al.*, the colossal spin valve effect is achieved when the Ni layer in their structure is rotated by an applied out-of-plane magnetic field to be perpendicular to the CrO<sub>2</sub> layer, generating spin-triplets. It is generally the case in thin-films that the geometry of the layers causes a lowering of  $T_c$  for out-of-plane fields compared to in-plane fields because of the increased orbital screening suppression when the field is out-of-plane. The orbital screening suppression can be removed to isolate spin-triplet contributions by measuring at zero applied field, however it is not always possible to maintain alignment of the ferromagnetic layers without a field, due to magnetic anisotropy. Therefore, Singh *et al.*<sup>66</sup> compared their spin valve to reference samples, such as single-layer S films, to isolate the spin-triplet component of their effect. Paschoa *et al.*<sup>51</sup> interpret their data on S–N bilayers in analogy to the colossal spin valve effect.

Because our samples undergo a similar rotation from in-plane to out-of-plane applied fields as those of Singh *et al.*, we discuss the ostensible analogy between the colossal spin valve effect and the orbital screening suppression in our trilayers. Equation 4 provides analytically  $T_c$  as a function of applied magnetic field. For this analysis, we consider only the high field data from Fig. 2 and Table 1, as this is where the changes in  $T_c$  with applied field are most pronounced. Next, we define a change of  $T_c$  between in-plane and out-of-plane applied

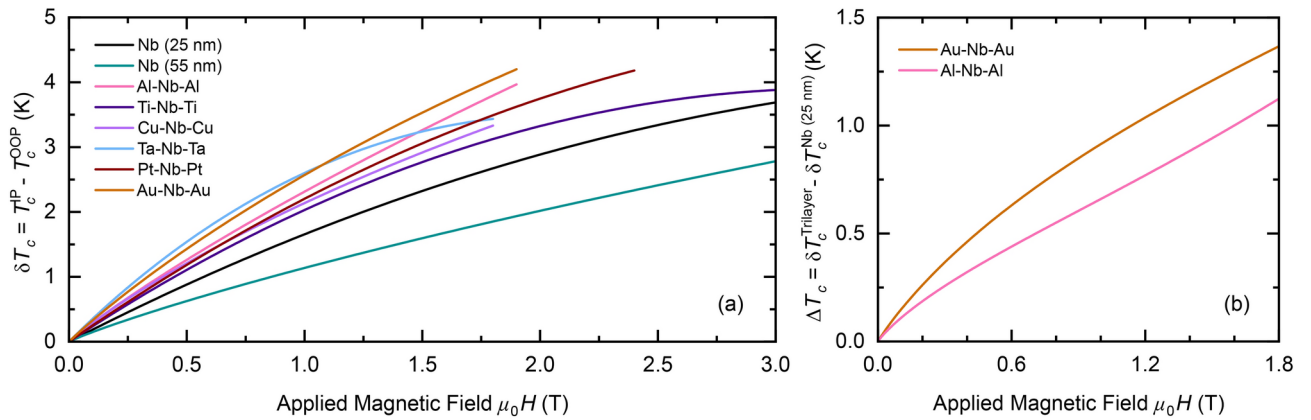


**Fig. 5.** Ostensible analogy with the colossal spin-valve effect. **(a)** The extracted change in critical temperature,  $\delta T_c$ , between in-plane and out-of-plane applied magnetic fields. The trilayers show a greater suppression of  $T_c$  compared to the single layer Nb films. **(b)** The difference in  $\delta T_c$  between the trilayers and 25 nm single layer Nb film,  $\Delta T_c$ , for the Au and Al trilayers.

fields as,  $\delta T_c = T_c^{\text{IP}} - T_c^{\text{OOP}}$ .  $\delta T_c$  is plotted for all samples in this study in Fig. 5a. We report that  $\delta T_c$  is greater for all trilayer films compared to single-layer Nb films, demonstrating that normal metals contribute an increase to the orbital screening suppression of  $T_c$ . The largest observed  $\delta T_c$  in the N–S–N trilayers is achieved for Au or Ta (depending on the applied field value) and smallest  $\delta T_c$  for Ti. At high fields, the Al trilayer shows the second largest suppression in  $T_c$ , highlighting that there is no trend in  $\delta T_c$  with the strength of spin–orbit interaction. To continue our analogy by comparing to a reference sample, we plot in Fig. 5b  $\Delta T_c$ , the difference between the trilayers with the single layer Nb for Au and Al. Doing so isolates only the contribution of additional suppression of  $T_c$  due to the presence of either Au or Al layers. Although our purely orbital screening effect is not a spin valve effect (it cannot manifest at zero applied field), it is interesting to note that the additional suppression due to the Au layers,  $\Delta T_c \approx 1.3$  K at 1.8 T, is greater than the additional suppression due to spin-triplets,  $\Delta T_c \approx 0.8$  K at 2.0 T, observed by Singh *et al.*<sup>66</sup>. In our trilayers,  $\delta T_c$  is clearly material dependent; however, there does not appear to be a clear trend indicating a role for normal metal resistivity or spin–orbit interaction, contradicting the conclusions of the recent work of Paschoa *et al.*<sup>51</sup> on Nb/Pt bilayers.

## Conclusions

In conclusion, we study a series of N–S–N trilayers with Al, Ti, Cu, Ta, Pt, and Au normal metals, along with single layers of Nb as reference, to probe the role of the proximity effect on the upper critical field of the trilayers. The upper critical fields of all our samples are well described by the standard Ginzberg–Landau functions, and we extract key parameters and trends from this framework. Trilayers with Ti, Ta, and Pt as well as a 25 nm thick Nb layer show responses to in-plane applied magnetic fields that are consistent with what would be expected for a 2-dimensional superconductor. We speculate that it is the higher resistivity of these normal metals, compared to Al, Cu, and Au, that causes a confinement of the superconductivity and hence the 2-dimensional behavior. We do not find strong trends in the critical temperatures or upper critical fields of the trilayers. The upper critical fields of the trilayers are suppressed relative to those of the Nb reference samples. At low applied magnetic fields and temperatures close to the zero field transition temperature, we found a possible deviation from 2-dimensional to 3-dimensional behavior in the Ti and Pt trilayers. We calculate the change in critical temperature of the trilayers under a rotation from in-plane to out-of-plane applied magnetic field and find that the trilayers have enhanced suppression of  $T_c$  during rotation relative to single layers of Nb. We discuss an ostensible analogy with the colossal spin-valve effect.

## Methods

The films were deposited in a single vacuum cycle using dc sputtering in a vacuum system with a base pressure of  $2 \times 10^{-8}$  Torr and a partial water pressure of  $3 \times 10^{-9}$  Torr after liquid nitrogen cooling. The samples were grown on 0.4 mm thick Si substrates with 100 nm thermal oxide. The growth was carried out at an approximate Ar pressure of 2 mTorr, at a typical growth rate of  $0.4 \text{ nm s}^{-1}$ . Growth rates were calibrated using an *in situ* crystal film thickness monitor to provide nominal layer thicknesses.

Resistivity measurements were performed in a Quantum Design Dynacool Physical Property Measurement System, equipped with a 9 T perpendicular field, and the Horizontal Rotator and Resistivity options. 4-point-probe electrical connections were made in a Van der Pauw geometry using either indium soldering or pressed contacts. For all measurements, a current of 1 mA was applied. The sample was rotated at a rate of  $1^\circ/\text{s}$  between in-plane and out-of-plane applied magnetic fields *in situ*.

## Data availability

The datasets generated during and/or analyzed during the current study are available in the Texas State University Dataverse Repository, <https://doi.org/10.18738/T8/0MGNEY>.

Received: 28 January 2025; Accepted: 10 April 2025

Published online: 16 April 2025

## References

1. Holm, R. & Meissner, W. Messungen mit Hilfe von flüssigem Helium. XIII. *Z. Phys.* **74**, 715–735. <https://doi.org/10.1007/BF01340420> (1932).
2. Meissner, H. Superconductivity of contacts with interposed barriers. *Phys. Rev.* **117**, 672–680. <https://doi.org/10.1103/PhysRev.117.672> (1960).
3. Clarke, J. The proximity effect between superconducting and normal thin films in zero field. *J. Phys. Colloq.* **29**, C2–C3. <https://doi.org/10.1051/JPHYSOL:1968201> (1968).
4. Eschrig, M. Spin-polarized supercurrents for spintronics. *Phys. Today* **64**, 43–49. <https://doi.org/10.1063/1.3541944> (2011).
5. Eschrig, M. Spin-polarized supercurrents for spintronics: A review of current progress. *Rep. Prog. Phys.* **78**, 104501. <https://doi.org/10.1088/0034-4885/78/10/104501> (2015).
6. Linder, J. & Robinson, J. W. A. Superconducting spintronics. *Nat. Phys.* **11**, 307–315. <https://doi.org/10.1038/nphys3242> (2015).
7. MeĤnikov, A. S., Mironov, S. V., Samokhvalov, A. V. & Buzdin, A. I. Superconducting spintronics: State of the art and prospects. *Phys. Usp.* **65**, 1248–1289. <https://doi.org/10.3367/UFNe.2021.07.039020> (2022).
8. Cai, R., Žutić, I. & Han, W. Superconductor/ferromagnet heterostructures: A platform for superconducting spintronics and quantum computation. *Adv. Quantum Technol.* **6**, 2200080. <https://doi.org/10.1002/qute.202200080> (2023).
9. Birge, N. O. & Satchell, N. Ferromagnetic materials for Josephson  $\pi$  junctions. *APL Mater.* <https://doi.org/10.1063/5.0195229> (2024).
10. Satchell, N. & Birge, N. O. Supercurrent in ferromagnetic Josephson junctions with heavy metal interlayers. *Phys. Rev. B* **97**, 214509. <https://doi.org/10.1103/PhysRevB.97.214509> (2018).
11. Satchell, N., Loloee, R. & Birge, N. O. Supercurrent in ferromagnetic Josephson junctions with heavy-metal interlayers. II. Canted magnetization. *Phys. Rev. B* **99**, 174519. <https://doi.org/10.1103/PhysRevB.99.174519> (2019).
12. Satchell, N. et al. Spin-valve Josephson junctions with perpendicular magnetic anisotropy for cryogenic memory. *Appl. Phys. Lett.* **116**, 022601. <https://doi.org/10.1063/1.5140095> (2020).
13. Satchell, N. et al. Pt and CoB trilayer Josephson  $\pi$  junctions with perpendicular magnetic anisotropy. *Sci. Rep.* **11**, 11173. <https://doi.org/10.1038/s41598-021-90432-y> (2021).
14. Komori, S. et al. Spin-orbit coupling suppression and singlet-state blocking of spin-triplet Cooper pairs. *Sci. Adv.* **7**, eabe0128. <https://doi.org/10.1126/sciadv.abe0128> (2021).
15. Kindiak, I., Mishra, S. S., Migliorini, A., Pal, B. & Parkin, S. S. Reduced decay in Josephson coupling across ferromagnetic junctions with spin-orbit coupling layers. *Appl. Phys. Lett.* <https://doi.org/10.1063/5.0214835> (2024).
16. Jeon, K.-R. et al. Enhanced spin pumping into superconductors provides evidence for superconducting pure spin currents. *Nat. Mater.* **17**, 499–503. <https://doi.org/10.1038/s41563-018-0058-9> (2018).
17. Jeon, K.-R. et al. Exchange-field enhancement of superconducting spin pumping. *Phys. Rev. B* **99**, 024507. <https://doi.org/10.1103/PhysRevB.99.024507> (2019).
18. Jeon, K.-R. et al. Tunable pure spin supercurrents and the demonstration of their gateability in a spin-wave device. *Phys. Rev. X* **10**, 031020. <https://doi.org/10.1103/PhysRevX.10.031020> (2020).
19. Flokstra, M. et al. Spin-orbit driven superconducting proximity effects in Pt/Nb thin films. *Nat. Commun.* **14**, 5081. <https://doi.org/10.1038/s41467-023-40757-1> (2023).
20. Banerjee, N. et al. Controlling the superconducting transition by spin-orbit coupling. *Phys. Rev. B* **97**, 184521. <https://doi.org/10.1103/PhysRevB.97.184521> (2018).
21. Martínez, I. et al. Interfacial spin-orbit coupling: A platform for superconducting spintronics. *Phys. Rev. Appl.* **13**, 014030. <https://doi.org/10.1103/PhysRevApplied.13.014030> (2020).
22. González-Ruano, C. et al. Superconductivity-induced change in magnetic anisotropy in epitaxial ferromagnet-superconductor hybrids with spin-orbit interaction. *Phys. Rev. B* **102**, 020405. <https://doi.org/10.1103/PhysRevB.102.020405> (2020).
23. Bregazzi, A. T. et al. Enhanced controllable triplet proximity effect in superconducting spin-orbit coupled spin valves with modified superconductor/ferromagnet interfaces. *Appl. Phys. Lett.* <https://doi.org/10.1063/5.0209305> (2024).
24. Niu, Z. A spin triplet supercurrent in half metal ferromagnet/superconductor junctions with the interfacial Rashba spin-orbit coupling. *Appl. Phys. Lett.* **101**, 062601. <https://doi.org/10.1063/1.4743001> (2012).
25. Bergeret, F. S. & Tokatly, I. V. Singlet-triplet conversion and the long-range proximity effect in superconductor-ferromagnet structures with generic spin dependent fields. *Phys. Rev. Lett.* **110**, 117003. <https://doi.org/10.1103/PhysRevLett.110.117003> (2013).
26. Bergeret, F. S. & Tokatly, I. V. Spin-orbit coupling as a source of long-range triplet proximity effect in superconductor-ferromagnet hybrid structures. *Phys. Rev. B* **89**, 134517. <https://doi.org/10.1103/PhysRevB.89.134517> (2014).
27. Konschelle, F. Transport equations for superconductors in the presence of spin interaction. *Eur. Phys. J. B* **87**, 119. <https://doi.org/10.1140/epjb/e2014-50143-0> (2014).
28. Jacobsen, S. H., Ouassou, J. A. & Linder, J. Critical temperature and tunneling spectroscopy of superconductor-ferromagnet hybrids with intrinsic Rashba-Dresselhaus spin-orbit coupling. *Phys. Rev. B* **92**, 024510. <https://doi.org/10.1103/PhysRevB.92.024510> (2015).
29. Alidoust, M. & Halterman, K. Spontaneous edge accumulation of spin currents in finite-size two-dimensional diffusive spin-orbit coupled SFS heterostructures. *New J. Phys.* **17**, 033001. <https://doi.org/10.1088/1367-2630/17/3/033001> (2015).
30. Alidoust, M. & Halterman, K. Long-range spin-triplet correlations and edge spin currents in diffusive spin-orbit coupled SNS hybrids with a single spin-active interface. *J. Phys. Condens. Matter* **27**, 235301. <https://doi.org/10.1088/0953-8984/27/23/235301> (2015).
31. Jacobsen, S. H., Kulagina, I. & Linder, J. Controlling superconducting spin flow with spin-flip immunity using a single homogeneous ferromagnet. *Sci. Rep.* **6**, 23926. <https://doi.org/10.1038/srep23926> (2016).
32. Costa, A., Högl, P. & Fabian, J. Magnetoanisotropic Josephson effect due to interfacial spin-orbit fields in superconductor/ferromagnet/superconductor junctions. *Phys. Rev. B* **95**, 024514. <https://doi.org/10.1103/PhysRevB.95.024514> (2017).
33. Hikino, S.-I. Magnetization reversal by tuning Rashba spin-orbit interaction and Josephson phase in a ferromagnetic Josephson junction. *J. Phys. Soc. Jpn.* **87**, 074707. <https://doi.org/10.7566/JPSJ.87.074707> (2018).
34. Simensen, H. T. & Linder, J. Tunable superconducting critical temperature in ballistic hybrid structures with strong spin-orbit coupling. *Phys. Rev. B* **97**, 054518. <https://doi.org/10.1103/PhysRevB.97.054518> (2018).
35. Montiel, X. & Eschrig, M. Generation of pure superconducting spin current in magnetic heterostructures via nonlocally induced magnetism due to Landau Fermi liquid effects. *Phys. Rev. B* **98**, 104513. <https://doi.org/10.1103/PhysRevB.98.104513> (2018).
36. Minutillo, M., Giuliano, D., Lucignano, P., Tagliacozzo, A. & Campagnano, G. Anomalous Josephson effect in S/SO/F/S heterostructures. *Phys. Rev. B* **98**, 144510. <https://doi.org/10.1103/PhysRevB.98.144510> (2018).
37. Johnsen, L. G., Banerjee, N. & Linder, J. Magnetization reorientation due to the superconducting transition in heavy-metal heterostructures. *Phys. Rev. B* **99**, 134516. <https://doi.org/10.1103/PhysRevB.99.134516> (2019).
38. Amundsen, M. & Linder, J. Quasiclassical theory for interfaces with spin-orbit coupling. *Phys. Rev. B* **100**, 064502. <https://doi.org/10.1103/PhysRevB.100.064502> (2019).

39. Eskilt, J. R., Amundsen, M., Banerjee, N. & Linder, J. Long-ranged triplet supercurrent in a single in-plane ferromagnet with spin-orbit coupled contacts to superconductors. *Phys. Rev. B* **100**, 224519. <https://doi.org/10.1103/PhysRevB.100.224519> (2019).
40. Vezin, T., Shen, C., Han, J. E. & Žutić, I. Enhanced spin-triplet pairing in magnetic junctions with *s*-wave superconductors. *Phys. Rev. B* **101**, 014515. <https://doi.org/10.1103/PhysRevB.101.014515> (2020).
41. Minutillo, M., Capecelatro, R. & Lucignano, P. Realization of  $0-\pi$  states in superconductor/ferromagnetic insulator/superconductor Josephson junctions: The role of spin-orbit interaction and lattice impurities. *Phys. Rev. B* **104**, 184504. <https://doi.org/10.1103/PhysRevB.104.184504> (2021).
42. Olde Olthof, L. A. B., Weggemans, J. R., Kimbell, G., Robinson, J. W. A. & Montiel, X. Tunable critical field in Rashba superconductor thin films. *Phys. Rev. B* **103**, L020504. <https://doi.org/10.1103/PhysRevB.103.L020504> (2021).
43. Aunsmo, S. & Linder, J. Converting a triplet Cooper pair supercurrent into a spin signal. *Phys. Rev. B* **109**, 024503. <https://doi.org/10.1103/PhysRevB.109.024503> (2024).
44. Amundsen, M., Linder, J., Robinson, J. W. A., Žutić, I. & Banerjee, N. Colloquium: Spin-orbit effects in superconducting hybrid structures. *Rev. Mod. Phys.* **96**, 021003. <https://doi.org/10.1103/RevModPhys.96.021003> (2024).
45. Kupriyanov, M. Y. Second critical field of two-layer films. *Sov. J. Low Temp. Phys.* **11**, 688–690. <https://doi.org/10.1063/10.0031401> (1985).
46. Fominov, Y. V. & Feigel'man, M. V. Superconductive properties of thin dirty superconductor-normal-metal bilayers. *Phys. Rev. B* **63**, 094518. <https://doi.org/10.1103/PhysRevB.63.094518> (2001).
47. Sidorenko, A. S., Sürgers, C. & Löhneysen, H. Perpendicular upper critical field of a proximity-coupled superconducting film. *Phys. C* **370**, 197–204. [https://doi.org/10.1016/S0921-4534\(01\)00929-7](https://doi.org/10.1016/S0921-4534(01)00929-7) (2002).
48. Cirillo, C. et al. Upper critical fields of Nb/Pd multilayers. *J. Low Temp. Phys.* **130**, 509–527. <https://doi.org/10.1023/A:1022435903243> (2003).
49. Kushnir, V., Prischepa, S., Cirillo, C. & Attanasio, C. Critical temperature and interface transparency of N/S/N triple layers: Theory and experiment. *EPJ B* **52**, 9–14. <https://doi.org/10.1140/epjb/e2006-00264-0> (2006).
50. Kushnir, V., Prischepa, S., Cirillo, C. & Attanasio, C. Proximity effect and interface transparency in Nb/Cu multilayers. *J. Appl. Phys.* <https://doi.org/10.1063/1.3267868> (2009).
51. Paschoa, A., Gonzalez, J. L., Checca-Huaman, N.-R., Nascimento, V. P. & Passamani, E. C. Colossal superconducting spin-valve effect in superconductor-non-magnetic metal heterostructure mediated by spin-orbit coupling. *Appl. Phys. Lett.* <https://doi.org/10.1063/5.0202337> (2024).
52. Clogston, A. M. Upper limit for the critical field in hard superconductors. *Phys. Rev. Lett.* **9**, 266–267. <https://doi.org/10.1103/PhysRevLett.9.266> (1962).
53. Chandrasekhar, B. S. A note on the maximum critical field of high-field superconductors. *Appl. Phys. Lett.* **1**, 7–8. <https://doi.org/10.1063/1.1777362> (1962).
54. Quarterman, P. et al. Distortions to the penetration depth and coherence length of superconductor/normal-metal superlattices. *Phys. Rev. Mater.* **4**, 074801. <https://doi.org/10.1103/PhysRevMaterials.4.074801> (2020).
55. Ptok, A., Rodriguez, K. & Kapcia, K. J. Superconducting monolayer deposited on substrate: Effects of the spin-orbit coupling induced by proximity effects. *Phys. Rev. Mater.* **2**, 024801. <https://doi.org/10.1103/PhysRevMaterials.2.024801> (2018).
56. Schneider, T. & Locquet, J.-P. Dimensional crossover and finite size effects in superconducting films. *Phys. C Supercond.* **179**, 125–130. [https://doi.org/10.1016/0921-4534\(91\)90020-Y](https://doi.org/10.1016/0921-4534(91)90020-Y) (1991).
57. Lenk, D. et al. Influence of the FFLO-like state on the upper critical field of a superconductor/ferromagnet bilayer: Angular and temperature dependence. *Phys. Rev. B* **93**, 184501. <https://doi.org/10.1103/PhysRevB.93.184501> (2016).
58. Weber, H. W. et al. Anisotropy effects in superconducting niobium. *Phys. Rev. B* **44**, 7585–7600. <https://doi.org/10.1103/PhysRevB.44.7585> (1991).
59. Tedrow, P. M. & Meservey, R. Critical magnetic field of very thin superconducting aluminum films. *Phys. Rev. B* **25**, 171–178. <https://doi.org/10.1103/PhysRevB.25.171> (1982).
60. Nam, H. et al. Ultrathin two-dimensional superconductivity with strong spin-orbit coupling. *PNAS* **113**, 10513–10517. <https://doi.org/10.1073/pnas.1611967113> (2016).
61. Oh, S., Youm, D. & Beasley, M. A superconductive magnetoresistive memory element using controlled exchange interaction. *Appl. Phys. Lett.* **71**, 2376–2378. <https://doi.org/10.1063/1.120032> (1997).
62. Tagirov, L. R. Low-field superconducting spin switch based on a superconductor/ferromagnet multilayer. *Phys. Rev. Lett.* **83**, 2058–2061. <https://doi.org/10.1103/PhysRevLett.83.2058> (1999).
63. Buzdin, A. I., Vedyayev, A. & Ryzhanova, N. Spin-orientation-dependent superconductivity in F/S/F structures. *EPL* **48**, 686. <https://doi.org/10.1209/epl/i1999-00539-0> (1999).
64. Fominov, Y. V. et al. Superconducting triplet spin valve. *JETP Lett.* **91**, 308–313. <https://doi.org/10.1134/S002136401006010X> (2010).
65. Mironov, S. V. & Buzdin, A. Standard, inverse, and triplet spin-valve effects in  $F_1/S/F_2$  systems. *Phys. Rev. B* **89**, 144505. <https://doi.org/10.1103/PhysRevB.89.144505> (2014).
66. Singh, A., Voltan, S., Lahabi, K. & Aarts, J. Colossal proximity effect in a superconducting triplet spin valve based on the half-metallic ferromagnet  $\text{CrO}_2$ . *Phys. Rev. X* **5**, 021019. <https://doi.org/10.1103/PhysRevX.5.021019> (2015).
67. Voltan, S., Singh, A. & Aarts, J. Triplet generation and upper critical field in superconducting spin valves based on  $\text{CrO}_2$ . *Phys. Rev. B* **94**, 054503. <https://doi.org/10.1103/PhysRevB.94.054503> (2016).
68. Feng, Z., Robinson, J. & Blamire, M. Out of plane superconducting Nb/Cu/Ni/Cu/Co triplet spin-valves. *Appl. Phys. Lett.* <https://doi.org/10.1063/1.4995434> (2017).
69. Kittel, C. *Introduction to solid state physics* 8th edn. (Wiley, 2004).

## Acknowledgements

We acknowledge experimental assistance through the Analysis Research Service Center from Sam Cantrell and Casey Smith. We acknowledge support from new faculty startup funding made available by Texas State University.

## Author contributions

N.S. conceived the study and wrote the manuscript. K.B.R. conducted the electrical transport measurements. K.B.R., A.J.H. and N.S. analyzed the data. P.S., R.M.K., R.L., N.O.B. and N.S. undertook the materials development and sample growth. All authors reviewed the manuscript.

## Declarations

## Competing interests

The authors declare no competing interests.

### Additional information

**Correspondence** and requests for materials should be addressed to N.S.

**Reprints and permissions information** is available at [www.nature.com/reprints](http://www.nature.com/reprints).

**Publisher's note** Springer Nature remains neutral with regard to jurisdictional claims in published maps and institutional affiliations.

**Open Access** This article is licensed under a Creative Commons Attribution-NonCommercial-NoDerivatives 4.0 International License, which permits any non-commercial use, sharing, distribution and reproduction in any medium or format, as long as you give appropriate credit to the original author(s) and the source, provide a link to the Creative Commons licence, and indicate if you modified the licensed material. You do not have permission under this licence to share adapted material derived from this article or parts of it. The images or other third party material in this article are included in the article's Creative Commons licence, unless indicated otherwise in a credit line to the material. If material is not included in the article's Creative Commons licence and your intended use is not permitted by statutory regulation or exceeds the permitted use, you will need to obtain permission directly from the copyright holder. To view a copy of this licence, visit <http://creativecommons.org/licenses/by-nc-nd/4.0/>.

© The Author(s) 2025